Supporting Information

Selenium speciation in framboidal and euhedral pyrites in shales

Adriana Matamoros-Veloza*, Caroline L. Peacock and Liane G. Benning*

Cohen Biogeochemistry Laboratory, School of Earth and Environment, University of Leeds, Leeds LS2 9JT, U.K (*corresponding author: A.MatamorosVeloza@leeds.ac.uk; L.G.Benning@leeds.ac.uk)

36 Pages

10 Tables

12 Figures

Table of Contents

List of Tables

List of Figures

1. Geological setting and bulk analyses of shale samples

All five shale samples (UK-1 to UK-5) are from West Yorkshire in the UK, but belong to three different geologic settings (**Table S1**).[1-2] Samples UK-1 and UK-2 are from the Upper Carboniferous, samples UK-3 and UK4 from the Lower Jurassic, and sample UK-5 is from the Upper Cretaceous. All five shales were deposited in shallow shelf seas in a stratified water column below the storm wave base. All formed in a setting with anoxic waters above the sediment-water interface and oxygenated waters near the surface and at water depths of between 200 to 400 meters.[3-5] Overall, in many settings shales have been identified as the most important source of Se in the environment derived through their weathering.[6] This is in part due to their high organic carbon (2-10%) and sulfide content (1-20% mainly as pyrite). In addition, shales contain variable amounts of silicate minerals (primarily clays, feldspars and quartz), and smaller amounts of carbonates[7-8] or sulfates.[6,9-10]

Table S1 Origin of samples and type(1-2)

Sample	Locality
UK-1	Nan Scar Beck Oxenhope, sample from the R2 goniatite zone
UK-2	Crimsworth Dean located to the north of Hebden Bridge, sample from the R1 goniatite zone)
UK-3	Port Mulgrave, sample from Middle Jet Rock; Paul Wignall sample collection number SNR 1064389
UK-4	Kettleness, sample from the Basal Jet Rock
UK-5	South Ferriby, sample from the Black Band in the Turonian

Table S2 CAS numbers and chemical formulas of standards used in μ-XANES analyses

Se standard	CAS No.	Chemical formula
6-Selenoinosine	40093-99-0	$C_{10}H_{12}N_4O_4Se$
Seleno-L-cysteine	29621-88-3	$C_6H_{12}N_2O_4Se_2$
Selenourea	630-10-4	NH_2CSeNH_2
Selenomethionine	1464-42-2	$C_6H_{11}NO_2Se$
Sodium selenate	13410-01-0	Na_aSeO_4
Sodium selenite	10102-8-8	Na_2SeO_3
Elemental Se (grey)	7782-49-2	Se
Copper selenide	1317-41-5	CuSe
Synthetic ferroselite*	-	$FeSe_2$
Se sulfide	7488-56-4	SeS_2
Berzelianite	-	$Cu_{1.8}Se$
Zinc selenide	131509-9	ZnSe

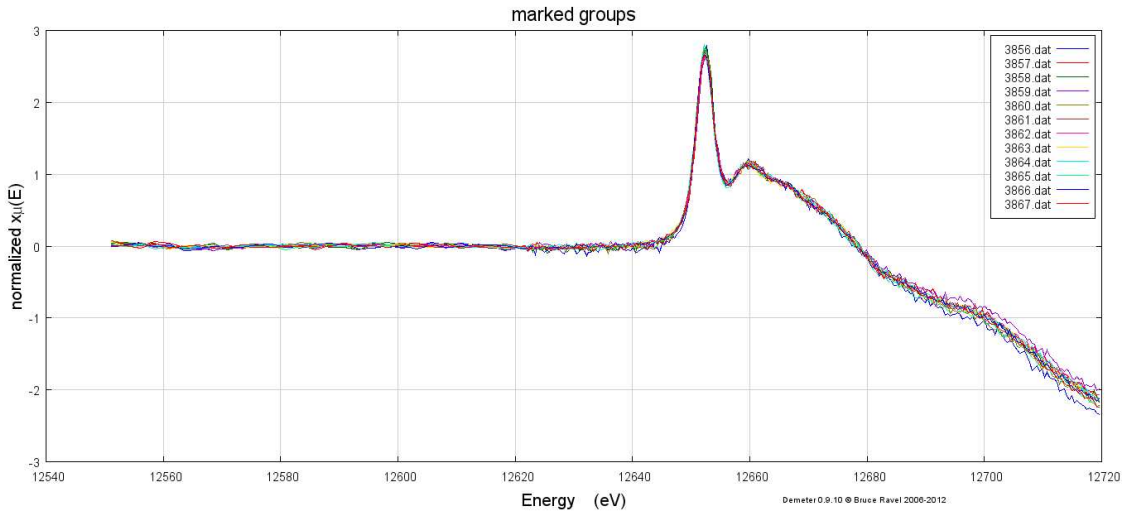

Figure S1 Twelve Se K-edge μ-XANES raw scans collected at POI 4.2 (see Table S3 below) showing no signs of oxidation or reduction.

Table S3 Summary of XAS analyses performed on Sample UK-2[a]

Area of Interest	XRF maps	POI	µ-XANES scans	µ-EXAFS scans
1	100 x 100 µm	1.1	4. Jump edge[b] 0.1	15 **(POI *a*)**
		1.2	4. Jump edge 0.06	No
		1.3	4. Jump edge 0.06	No
2	150 x 150 µm	2.1	2. No good scans	No
		2.2	2. No good scans	No
		2.3	2. No good scans	No
3	750 x 400 µm	3.1	4. Jump edge 0.08	No
		3.2	4. Jump edge 0.08	No
		3.3	2- No good scans	No
		3.4	4. Jump edge 0.04	No
		3.5	4. Jump edge 0.01	No
4	100 x 100 µm	4.1	1. No good scan	No
		4.2	12. Jump step 0.03	No
		4.3	1. No good scan	No
		4.4	1. No good scan	No
		4.5	1. No good scan	No
5	350 x 450 µm	5.1	4. Jump edge 0.12	16 **(POI *b*)**
		5.2	4. Jump edge 0.05	No
		5.3	4. Jump edge 0.10	3[c]
		5.4	4. Jump edge 0.12	No
		5.5	4. Jump edge 0.07	No
		5.6	4. Jump edge 0.07	No

[a]Attempts were made in analysing other samples from this study but they were unsuccessful as the concentration of Se was not high enough to provide quality of data.

[b] Jump edge= absorption length

[c] Intended to collect 16 scans but these 3 showed a diffraction peak

2. Elemental composition

Table S4 shows the composition of the samples (and standards) measured by bulk XRF. Analyses were performed using an ARL 9400 wavelength dispersive, sequential X-ray fluorescence spectrometer (XRF) with an Rh tube (School of Geosciences, University of Edinburgh). The standard reference materials BHVO-1 and MAG-1 were also analysed in duplicate to evaluate the quality of the measurements. The Fe_2O_3 content in all samples varied between ~2 and ~6% and CaO was typically < ~ 2% except for sample UK-5 with 35%. This sample also had the highest total C content (8.7% - see **Table S4** below) reflecting the abundance of calcite in this sample as confirmed by XRD (**Table S5**). The total SiO_2 contents indicate a fairly low proportion of quartz in these samples as also confirmed by the quantitative XRD analyses **Table S5**.

Table S4 Elemental composition derived from the bulk XRF measurements of the five samples and selected standards (including certified values) reported as oxides.

Elemental composition as oxides (%)									
	Samples					Standards			
Sample	UK-1	UK-2	UK-3	UK-4	UK-5	BHVO-1	Cert.	MAG-1	Cert.
SiO_2	48.9	49.3	44.8	45.3	22	50.15	49.9	49.2	50.4
TiO_2	0.8	0.9	0.9	0.9	0.3	2.7	2.7	0.7	0.8
Al_2O_3	23.5	24.9	21.1	18.3	6.9	13.6	13.8	16	16.4
Fe_2O_3	6.5	5.5	7.2	9.1	1.9	12.3	12.2	6.7	6.8
Mn3O4	0.02	0.02	0.02	0.02	0.02	0.6	0.6	0.1	0.1
MgO	1.5	1.1	1.3	1.3	1.2	7.2	7.2	3	3
CaO	-	0.03	3.3	1.8	35.2	11.3	11.4	1.3	1.4
Na_2O	-	-	0.3	0.3	-	2.2	2.3	3.7	3.8
K_2O	3.5	2.8	3.1	2.7	1.4	0.5	0.5	3.5	3.6
P_2O_5	0.07	0.1	0.2	0.2	0.4	0.3	0.3	0.2	0.2
Total as oxides	84.8	84.6	82.3	79.9	69.2	100.8	100.9	84.45	86.3
LOI @ 1025°C	13.65	13.8	15.78	18.3	33.77	-	- -	-	-
Total	98.4	98.4	98.1	98.2	103	-	- -	-	-

3. Mineralogical composition

Table S5 shows the main minerals present in the samples with representative XRD patterns of samples (UK-2) in the insert panel. All samples contained kaolinite, quartz, feldspars, pyrite and illite-smectite but sample UK-5 revealed a high proportion of calcite matching the bulk XRF analyses (**Table S4**). In contrast to all other samples in sample UK-5 no pyrite could be identified.

All samples were analysed as homogenized powders (<53μm) using a Phillips PW1050 X-ray diffractometer with a Cu tube (Cu Kα radiation) and a graphite monochromator. Patterns were collected in the 2-theta range from 5 to 70º with a 0.02º step size and a 1º/min sampling time. The mineralogical composition (i.e., relative percentage of phases) was quantified using Rietveld refinement and the software package Topas; v.4.2 (copyright 1999–2009 Bruker AXS).

Table S5 Quantitative mineralogical composition of the shale samples normalized to 100% as derived from Rietveld refinement of the XRD spectra between 9-70 2-Theta degrees. Diffraction features below 9 2-Theta degrees were assigned to 2:1 intergrade clays but they were not included in the refinement. The Rietveld refinement plots are in **Figure S2**.

Mineralogical composition (%)					
Sample	UK-1	UK-2	UK-3	UK-4	UK-5
Albite	-	-	-	-	1.9
Anorthite	-	3.5	-	-	-
Calcite	-	-	-	-	40.0
Chlorite	10.1	9.7	15.8	12.4	1.2
Gypsum	-	-	0.7	1.1	-
Kaolinite	9.2	10.6	9.8	8.6	-
Microcline	25.8	22.1	25.5	26.7	-
Montmorillonite	-	-	-	-	40.0
Illite	42.9	41.5	34.6	28.1	19.0
Pyrite	1.5	1.4	2.7	4.9	-
Quartz	10.5	11.2	11.1	18.2	4.0
Silicates+Quarz	98.5	95.1	96.8	94.0	66.1

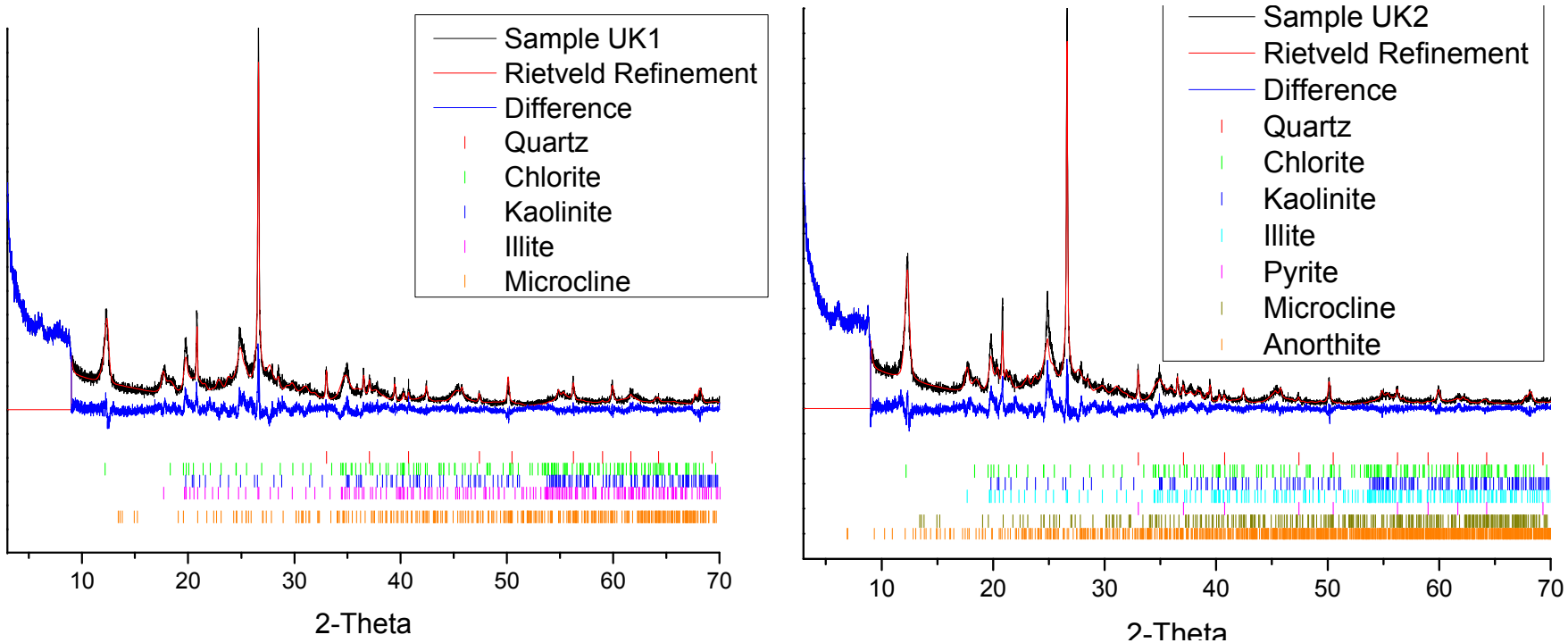

Figure S2 Rietveld refinement plots for UK samples

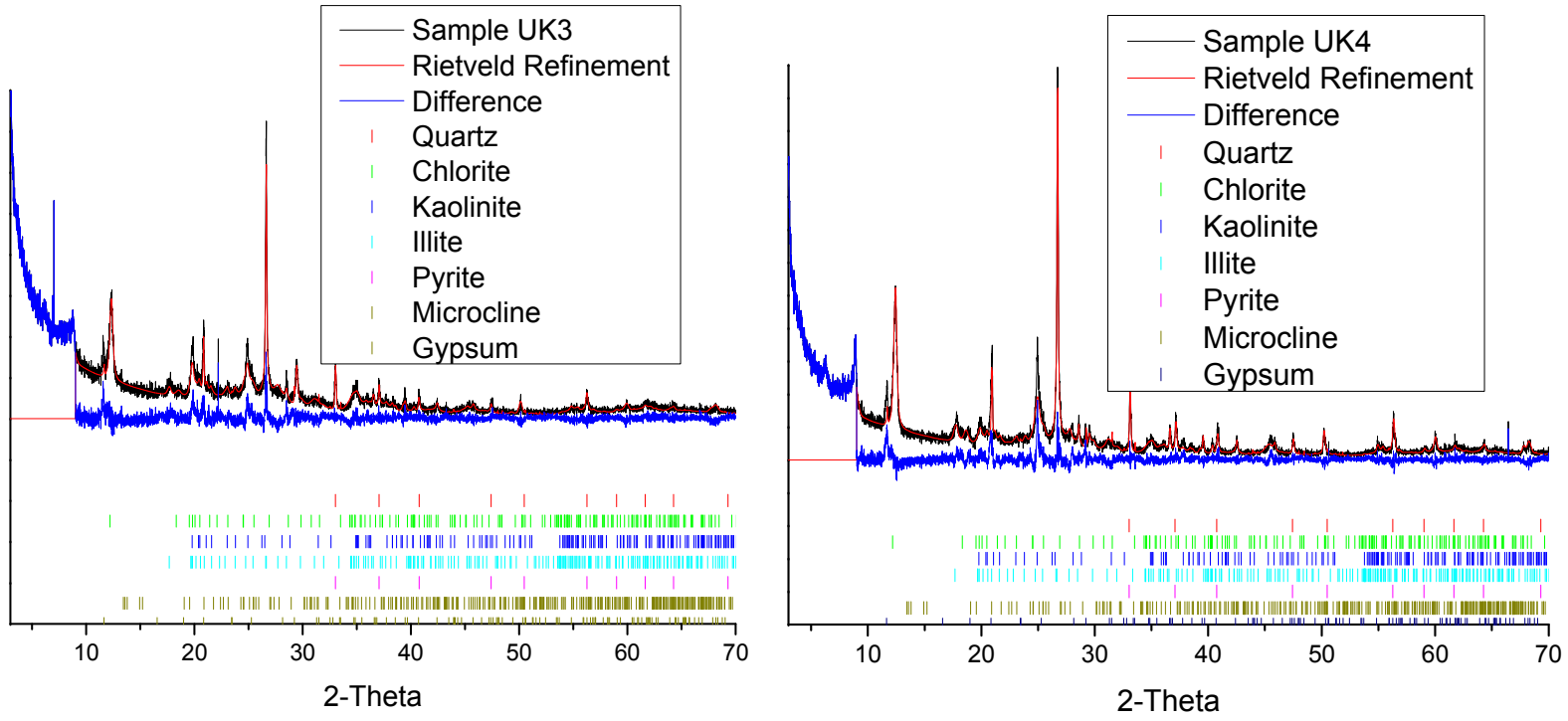

Figure S2 (cont.) Rietveld refinement plots for UK samples

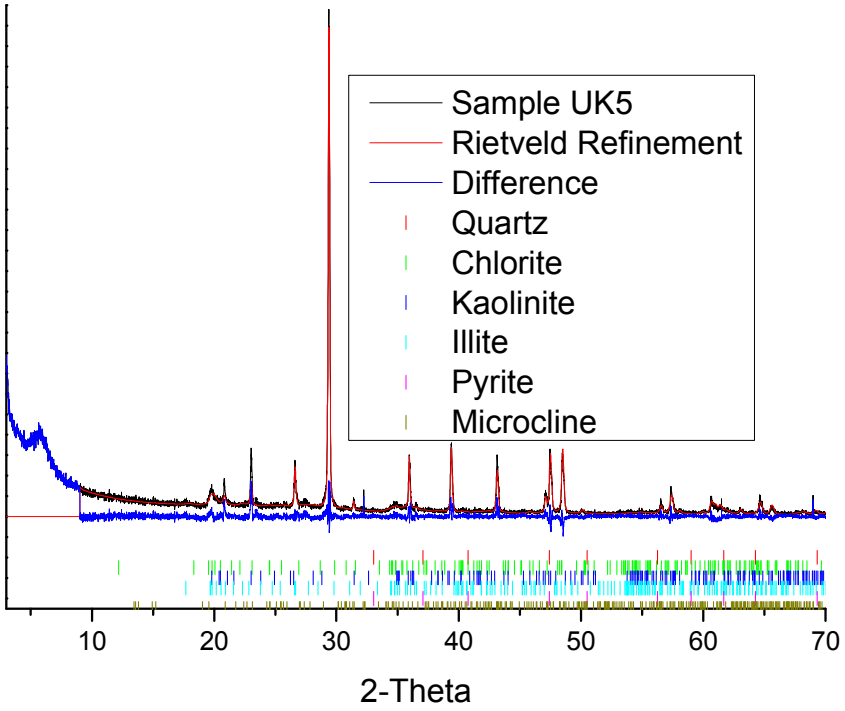

Figure S2 (cont.) Rietveld refinement plots for UK samples

4. Bulk characterisation

For the total bulk Se analyses, the samples were fully digested using a microwave assisted reaction system (MARS). The digestion used concentrated nitric acid, hydrofluoric acid and hydrogen peroxide mix. The MARS was run at a power of 840W, a pressure of 350 PSI and a ramp of 10 minutes to reach 180ºC. The temperature was held for 10 minutes to completely digest the powered samples (≤152µm). Quality of the digestion method and analyses was controlled with the inclusion of a reference material (PACS-1). The derived solutions were analysed using hydride generation graphite furnace (Hydrea) absorption spectroscopy (HG-AAS; High Resolution Continuum Source, ContrAA 700 Analytik Jena). The analyses were performed with a precision <8% using 7 replicates of digestion and 3 replicates of measurement. The reference material yielded a mean value for concentration of 1.07µg/g and the certified value is 1.09µg/g.

Total C and S were measured directly by elemental analysis (isotope ratio mass spectrometry/EA-IRMS; Euro EA3000-Micromass Isoprime Eurovector, Milan). Reduced inorganic sulfur was determined by chromous chloride reduction following the methods of Newton et al. [(11)]

Total organic carbon (TOC) was measured by elemental analysis with isotope ratio mass spectrometry (EA-IRMS) after removal of carbonates with HCl.

Table S6 compiles the total digest results for bulk Se, as well as the analyses for S and C in all five samples. The bulk Se concentrations varied between 0.83 and 9.77µg/g, while the total reduced inorganic sulfur varied between 1.28 and 2.75%, which represents in most cases ~ 50-70% of the total sulfur in the sample. Sample UK – 5 contained no inorganic reduce sulfur, thus confirming the absence of pyrite or other reduced sulfides as suggested by the XRD analyses above (**Table S5**). Note the high total carbon content in sample UK-5, confirming the high % of calcite in this sample (**Table S5**)

Table S6 Bulk Se concentration, carbon and sulfur results.

Sample	UK-1	UK-2	UK-3	UK-4	UK-5
Bulk Se (µg/g)	3.13	9.77	1.29	0.83	3.87
Total Carbon	2.6	2.1	4.6	5.9	8.7
Total Organic C (TOC) (%)	2.1	1.7	3.0	5.1	2.0
Se/TOC	2.27×10^{-05}	8.74×10^{-05}	6.54×10^{-06}	2.48×10^{-06}	2.94×10^{-05}
Total S (%)	1.83	1.7	2.72	4.68	0.03
Reduced Inorg S (%)	1.31	1.28	1.6	2.75	-
Inorg S/ Total S	0.72	0.75	0.59	0.59	-

5. Trace elements analyses

Table S7 shows the trace element concentrations determined by a near total microwave digestion (HF-$HClO_4$-HNO_3-HCl) and quantification using an inductively coupled plasma mass spectrometer (ICP-MS, Perkin Elmer Sciex ELAN instrument) carried out by Activation Laboratories Ltd (ActLabs – Canada). The digestion and analyses followed the protocols established by Actlabs, namely sample digestion using the acid mixture with controlled heating until dryness, then re-solubilisation with HCl/HNO_3. The quality of the analyses was evaluated with five standard reference materials (GXR-1, GXR-4, GXR-2, GXR-6 -USGS) for the digestion and measurement processes.

Sample UK-2 showed higher Mn, Cu and As concentrations than the other samples. The Mn contents may reflect an association of Mn with aluminosilicate/ clay minerals inferred to be present from the major element analyses above; Cu and As could be associated with the organic matter or the pyrite in this sample. [12] Elements that gave values close to the certified values are shaded; elements that differ in some cases by between 20 and 40% from the certified values are shown in white. Spearman correlations were significant at the 0.05 level (2-tailed) using enrichment factors, which were calculated as $(Element/Al)/(Element/Al)_{shale}$. [12]

Table S7 Concentration of trace elements in the five shale samples and in the standard reference materials analysed. *Element concentrations that were used as indicative values but had a recovery rate of ~ 80%.

Trace elements (µg/g)														Detection Limit	Spearman Correlations
	Samples					Standards									
Sample	UK-1	UK-2	UK-3	UK-4	UK-5	GXR-1	Cert.	GXR-2	Cert.	GXR-4	Cert.	GXR-6	Cert.		
Bulk Se	3.13	9.77	1.29	0.83	3.87	18.6		0.74		6.0		1.07			
V	124	161	124	129	208	78	80	49	52	87	87	186	186	1.0	0.81
Cr*	154	126	113	117	54	10.6	12	29.7	36	49.7	64	78.7	96	0.5	0.83
Mn*	208	251	215	236	216	809	852	588	1010	154	155	800	1010	1.0	-
Ni	100	97	117	85	116	42.9	41	19.4	21	41.3	42	25.7	27	0.5	0.78
Co	25.1	21.9	28.8	21.5	60	8.6	8.2	8.6	8.6	14.6	14.6	13.8	13.8	0.1	_
Mo	10.8	6.1	18.3	3.9	0.6	18.3	18	1.2	2.1	310	310	2.1	2.4	0.1	_
Cu*	122	118	53	61	95	1490	1110	104	76	6230	6520	93.8	66	0.2	0.76
As	13	16	12	12	3	431	427	96.9	98	25.1	25	313	330	0.1	_

6. Sequential extractions and total digestion in the residual fraction

Figure S3 illustrates the measured Se distribution using the two operationally defined protocols for Se extraction. Protocol A (Top: Kulp and Pratt, modified)[13] and Protocol B (Bottom: Lussier et al. [14]). A detailed description of these protocols is described in Matamoros et al. [15] The chromous chloride reduction allowed differentiation of Se between the organic matter and sulfides (**Figure S4**). The comparison between the Se associated with organic matter and sulfides in all extraction protocols shows that between 20% and 75% of the bulk Se was associated with the sulfides. A detailed description of these protocols is given in Matamoros et al. [15]

To determine the Se concentration in the residual fractions of each protocol a full digestion of this fraction, using the same approach as applied to the bulk sample above (MARS) was applied. The resulting solutions from each extraction step were analysed for Se concentrations by hydride generation graphite furnace atomic absorption spectroscopy (HF-AAS). Triplicates for each sample and standards were run and a QC sample was included every 10 samples.

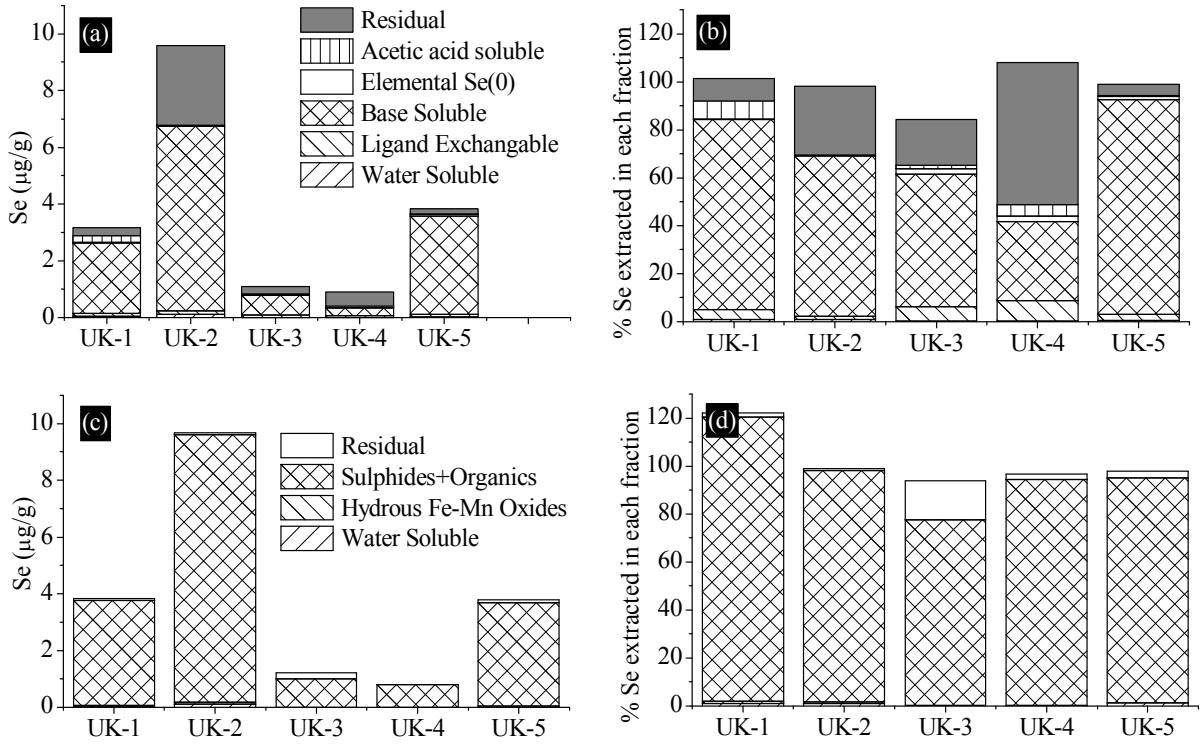

Figure S3 Distribution of selenium in the operationally extracted fractions. Protocol A, (a) in concentration and (b) in percentage. Protocol B, (c) in concentration and (d) in percentage.

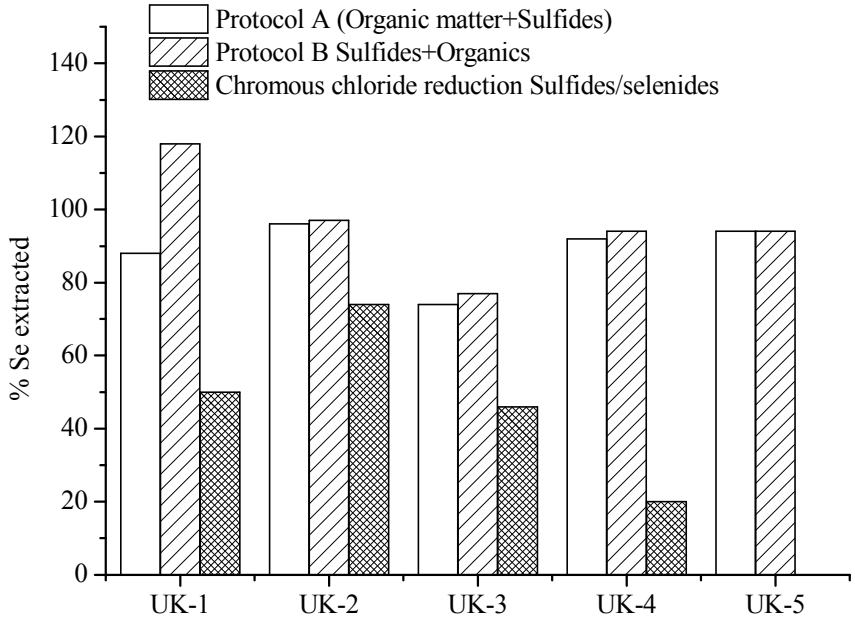

Figure S4 Percentage of Se associated with the sulfide and organic matter fractions in Protocols A and B, and associated with sulfides/selenides from the chromous chloride reduction. Note absence of sulfides/selenides in sample UK-5 and high proportion of sulfides in sample UK-2.

7. Se concentrations in individual pyrite grains evaluated by electron microprobe analysis (EMPA)

The morphologies of individual sulfide grains (both euhedral and framboidal) were imaged with a CamScan Series 4 Scan electron microscope fitted with an Oxford Microanalysis X-ray energy dispersive system (EDX) operated at 20kV and 50nA. After identification and assessment of the predominant types of sulfide morphology, we analysed Se concentrations in pyrite grains and at a few control points on the silicate and organic matrices. The electron microprobe analyses were performed using a Cameca SX-50 electron microprobe, fitted with three X-ray wavelength dispersive spectrometers and operated at 20kV and 50nA. Counts were 120s for Se on peak and 60s at each of two background positions.

Overall, the concentration of Se in individually analysed pyrite grains (regardless whether framboidal or euhedral, **Table S8**) was typically ~ 1-3 orders of magnitude higher than the measured bulk concentration in the same sample. This was true even when taking into consideration the fact that the EMPA analyses are semi-quantitative, and that in some cases the absolute Se concentration values may have been affected by matrix effects. The Fe and S analyses revealed in all cases a Fe:S ratio close to pyrite of 1:2. However, based on the Si concentrations also analysed at each point, a maximum 7% contribution of Si to the total analyses was found in a few of the analysed pyrite grains. This was in contrast to the average of ~ 30% Si measured when analyses were carried out on silicates in the matrix.

Table S8 Electron microprobe data for Se concentrations in framboidal and euhedral pyrite grains (ppm) in each sample; the wt% Si and the normalized atomic data for iron and sulfur are also shown*.

Bulk Se UK-1 sample = 3.13 ppm							
Framboidal point analyses				Euhedral point analyses			
Se, ppm	Si, wt %	Fe*	S*	Se, ppm	Si, wt %	Fe*	S*
<LD	0.1	33	67	300	2.7	32	64
180	1.5	33	65	260	2.8	32	64
220	1.6	33	65	320	0.7	33	66
300	0.8	33	66	390	1.0	33	66
<LD	0.6	33	66	380	1.0	33	66
110	0.8	33	66	110	0.2	33	66
220	0.6	33	66	370	2.0	32	65
140	0.9	33	66	430	0.7	33	66
200	1.9	32	65	170	0.1	33	67
200	0.1	33	67	561	0.7	33	66
240	5.9	31	61	100	1.3	33	65
<LD	3.2	32	64	160	0.5	33	66
<LD	1.5	33	65	400	0.3	33	66
<LD	1.3	33	65	250	1.0	33	66
110	0.2	33	66	-	-	-	-

Bulk Se UK-2 sample = 9.77 ppm							
Framboidal point analyses				Euhedral point analyses			
Se, ppm	Si, wt %	Fe*	S*	Se, ppm	Si, wt %	Fe*	S*
<LD	0.5	33	66	<LD	0.8	33	66
<LD	0.3	33	66	602	0.1	33	67
361	0.1	33	67	427	0.6	33	66
238	0.2	33	66	226	0.4	32	65
179	0.1	33	67	272	1.7	33	65
256	0.3	33	66	448	0.1	33	67
<LD	1.1	33	66	312	0.3	33	66
437	0.2	33	66	235	4.6	31	63
300	1.5	33	65	190	0.5	33	66
114	0.2	33	67	523	1.1	33	66
389	1.3	33	65	533	0.5	33	66
510	0.6	33	66	670	2.2	32	65
<LD	0.5	33	66	270	2.3	32	65
<LD	0.3	33	66	590	0.2	33	66
260	0.4	33	66	-	-	-	-
370	0.2	33	66	-	-	-	-
370	0.4	33	66	-	-	-	-
360	0.4	33	66	-	-	-	-
430	0.6	33	66	-	-	-	-
240	0.2	33	66	-	-	-	-
180	0.1	33	67	-	-	-	-
260	0.3	33	66	-	-	-	-
<LD	1.1	33	66	-	-	-	-
300	1.5	31	63	-	-	-	-
440	0.2	33	66	-	-	-	-
110	0.2	33	66	-	-	-	-
390	1.3	33	66	-	-	-	-

Bulk Se UK-3 sample = 1.29 ppm							
Framboidal point analyses				Euhedral point analyses			
Se, ppm	Si, wt %	Fe*	S*	Se, ppm	Si, wt %	Fe*	S*
250	0.1	33	67	-	-	-	-
<LD	0.1	33	67	-	-	-	-
<LD	0.1	33	67	-	-	-	-
<LD	0.2	33	67	-	-	-	-
<LD	0.1	33	67	-	-	-	-
<LD	0.1	33	67	-	-	-	-
110	0.1	33	67	-	-	-	-
120	0	33	67	-	-	-	-
310	0	33	67	-	-	-	-
130	0	33	67	-	-	-	-
<LD	0.1	33	67	-	-	-	-
170	0	33	67	-	-	-	-
130	0.1	33	67	-	-	-	-
<LD	0.1	33	67	-	-	-	-
<LD	0.1	33	67	-	-	-	-
<LD	0.1	33	67	-	-	-	-
<LD	0.3	33	66	-	-	-	-
150	0.1	33	67	-	-	-	-
<LD	0.1	33	67	-	-	-	-
<LD	0.6	33	66	-	-	-	-

Bulk Se UK-4 sample = 0.83 ppm							
Framboidal point analyses				Euhedral point analyses			
Se, ppm	Si, wt %	Fe*	S*	Se, ppm	Si, wt %	Fe*	S*
<LD	0.2	33	67	160	2.1	33	66
<LD	0.2	33	66	150	1.0	33	65
<LD	0.1	33	67	200	1.3	32	64
<LD	0.1	33	67	150	3.1	32	65
<LD	1.2	32	65	170	1.8	32	64
<LD	0.6	33	66	<LD	3.0	33	66
<LD	4.1	31	63	<LD	0.5	30	61
<LD	2.5	64	100	120	7.0	32	64
<LD	1.8	32	65	200	2.8	33	66
<LD	0.1	33	67	200	1.8	30	61
<LD	3.6	32	63	<LD	1.0	33	67
<LD	0.1	33	67	120	1.2	32	64

No data for UK-5 as this sample does not contain pyrite (**Table S5** and **Table S6**).

8. Beamline set up and data processing

The optical scheme for beamline I18 consists of three sets of mirrors and a liquid nitrogen-cooled double crystal monochromator composed of two sets of silicon crystals [Si(111) and Si(311)]. The station is equipped with a 9-element solid-state detector optimised for energies above 5 keV. The monochromator energy was calibrated with Au foil before all measurements and after the first calibration the K-edge energy for trigonal Se(0) was determined to be 12650 eV. We note this is less that the tabulated value for Se(0) (12658 eV),[16] and all our data were thus shifted by 8 eV to calibrate with the theoretical value. The accuracy of the monochromator was ±0.1 eV.

To be able to quantify the oxidation state of Se in the analysed POI, we collected μ-XANES and EXAFS spectra of 11 Se standards. Standards covered four different nominal oxidation states: (a) Se (-II) in SeS_2, CuSe, ZnSe, $Cu_{1.8}Se$, (b) Se(0) in grey elemental Se, (c) Se(IV) in Na_2SeO_3, (d) Se(VI) in Na_2SeO_4, (e) organic Se species in 6-Selenoinosine (C=Se), Seleno-L-cysteine (R-Se-Se-R), Selenomethionine (R-Se-CH_3) and selenourea (C=Se). Standards were diluted to 6 % Se using boron nitride and pressed into pellets. XAS information (2 scans) from the standards was collected in transmission mode, whereas samples were measured as polished thin sections in flourescence mode.

We processed the μ-XRF data using the software PyMCA[17] for background correction and to produce quantitative elemental maps. We used the software package SMAK[18] to extract fluorescence data and to construct elemental correlation plots. For analysis of the μ-XANES spectra, we calibrated, averaged multiple spectra collected at each POI, normalized and plotted our data using ATHENA,[19] PySpline v1.3[20] and Origin Pro v8 (copyright 1991-1998 Origin Lab Corporation). μ-XANES sample spectra were

compared to the XANES of the standards taking as reference the inflection point of the first derivative, the position of the white line peak at the absorption rate, and the feature "A" or second absorption peak. The spectra and standards were compared using the inflection point of the first derivative, the position of the white line peak at the absorption edge and the second peak of the XANES oscillations as reference. We extracted the μ-EXAFS sample spectra using the AUTOBK algorithm implemented in ATHENA[19] and then we made attempts to fit the spectra to Se coordination environments as found in seleno-L-cysteine, selenium sulfide, elemental selenium, pyrite and ferroselite ($FeSe_2$) using ARTEMIS[18] which implements the FEFF8 and IFEFFIT codes.[19] EXAFS goodness of fit was assessed using the reduced Chi^2 and the R-factor.[21]

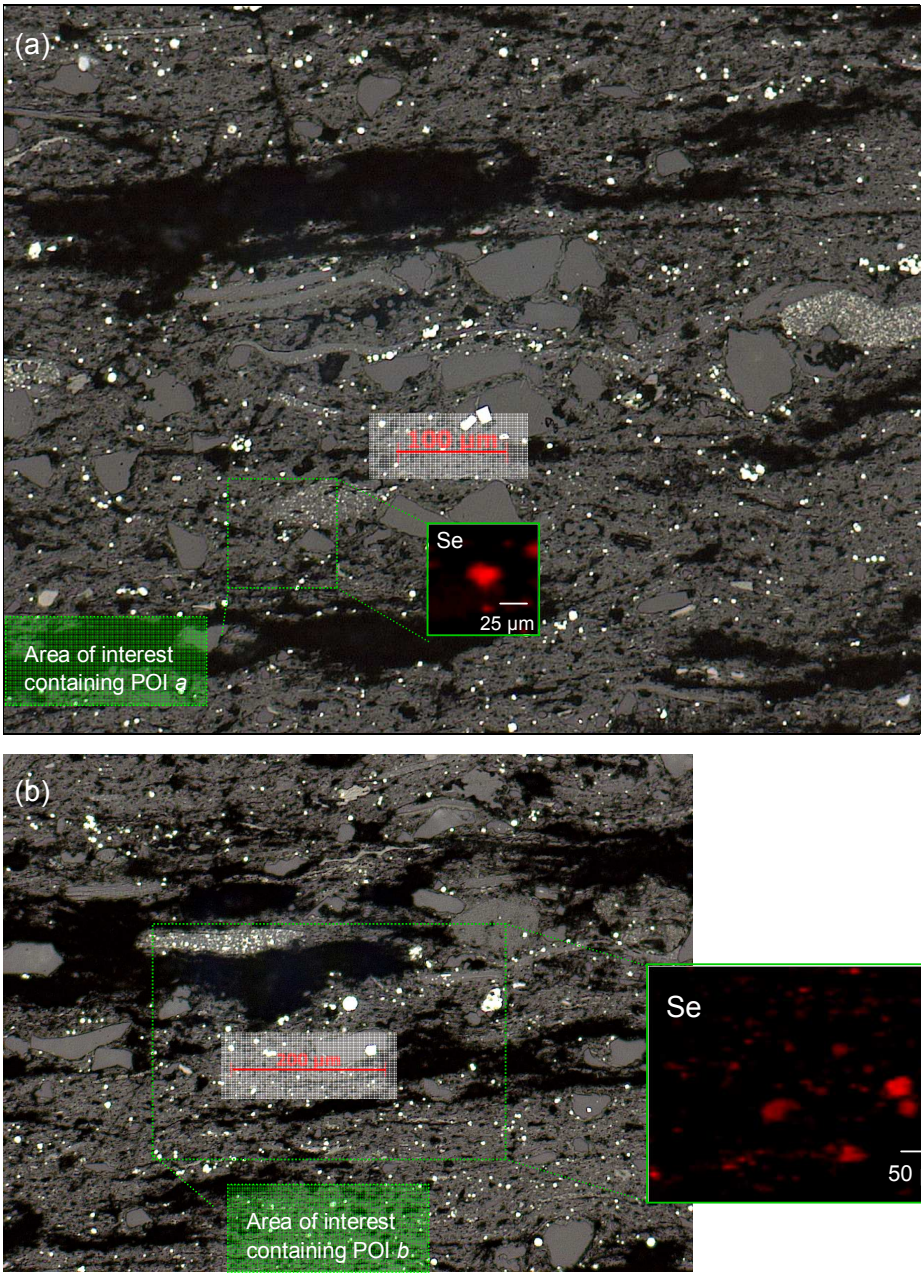

Figure S5 Images of sample UK-2 with mapped areas and localized POI where XAS analyses were carried out. (a) area including POI a (b) area including POI b. Overlain are the respective Se distribution maps.

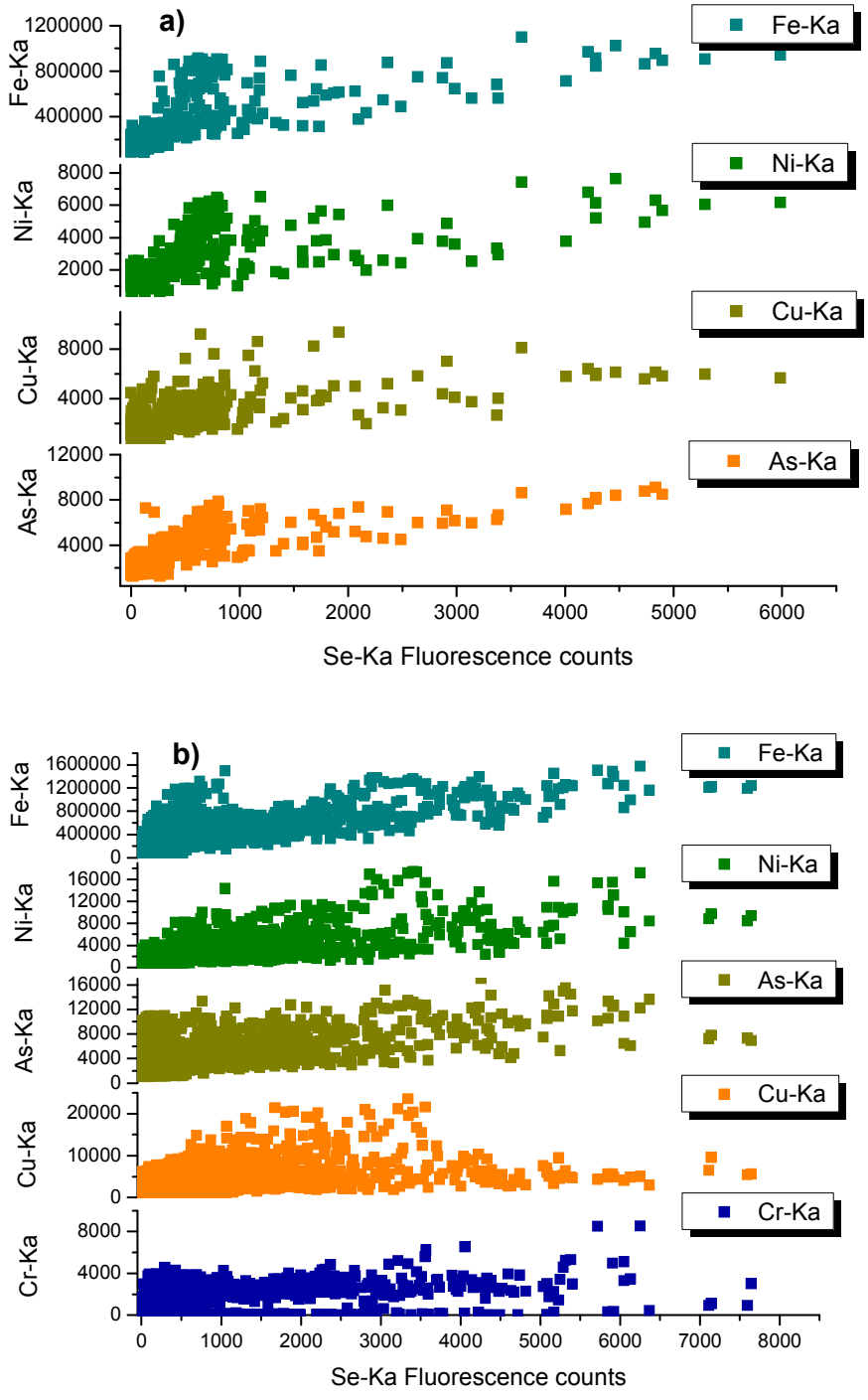

Figure S6 Bi-variated Pearson correlations between Se and Fe, Ni, Cu, As in areas of interest containing a) POI$a_{euhedral}$ and b) POI$b_{framboidal}$. Correlations calculated pixel-by-pixel from the µ-XRF fluorescence maps. Both POI showed strong and positive correlations between Se-Fe, Se-Ni, Se-Cu and Se-As.

Table S9 Pearson correlations (significant at the 0.01 level, 2-tailed) for Se and Fe with Ni, Cu, As, Cr and Zn in the μ-XRF mapped areas of interest including points of interest (POI) *a* and *b*. Correlations are based on all fluorescence counts from each map, analysed pixel-by-pixel, and not only with the counts at a specific POI.

		Area of interest including POI $a_{euhedral}$	Area or interest including POI $b_{framboidal}$
	Number of data points/pixels	400	5824
Se	Fe	0.63	0.75
	Ni	0.61	0.73
	Cu	0.62	0.56
	As	0.75	0.63
	Cr	-	0.58
Fe	Se	0.63	0.75
	Ni	0.94	0.86
	Cu	0.54	0.60
	As	0.88	0.55
	Cr	0.54	0.58
	Zn	-	0.18

9. μ-XANES analyses

Table S10 and **Figure S7** (left side) show the Se K-edge absorption energies (at the inflection point and white line) and the μ-XANES spectra for the standards, respectively. Looking at the variation in the edges of the Se(-II, 0) inorganic species in **Figure S7**, it is evident that the XANES edge positions and spectral shapes depend not only on Se oxidation state, but also on the chemical environment of Se: including coordination chemistry (i.e., trigonal, cubic), crystalline vs. aqueous forms, different allotropes and resultant multiple scattering effects.[22] In a similar manner to the inorganic standards, Se(-II) in the organic species can be differentiated using the same criteria (i.e., first inflection point, main edge position and additional features like a second characteristic peak, **Figure S7**).

With increasing Se electron valance (from VI to –II) the intensity of the main peak is clearly reduced, reflecting the population of the valence 4p levels.[22] In addition, the edge position is shifted to lower energies (i.e., first inflection point of Se(VI) at 12665.4eV and Se(0) at 12658.0eV), reflecting the change in effective nuclear charge.[22] The edge positions, for Se(VI) and (IV) were at 12665.4 and 12662.3eV, respectively, whereas the edge positions for Se(0) in elemental Se and Se(-II) in SeS_2 were at lower energies (i.e., 12658.0 and 12658.1eV, respectively). The difference between Se(-II, 0) and Se(IV) was 4.2eV, and in relation to Se(VI) it was 7.3eV making it possible to clearly distinguish the reduced species from the oxidased species. We included the synthetic ferroselite [Se(-I) from Ryser et al.[23]] for comparison (**Table S10** and **Figure S7**). It should be noted that the XAS analysis conditions in the Ryser et al.[23] study were different to the current study and thus their ferroselite spectrum is most likely shifted in edge energy compared to those here. However, differing analysis conditions will not alter the overall spectral fingerprint of the XANES and EXAFS regions and therefore the Ryser ferroselite spectrum constitutes a satisfactory reference spectra for Se(-I).

The plots on the right in **Figure S7** show the Se K-edge EXAFS oscillations ($\chi k*k3$) of the standards as a function of the photoelectron wavenumber (1/Å). These, in addition to the XANES spectra, were also used to fingerprint the Se chemical coordination environment in the samples (i.e., coordination numbers and bond lengths).

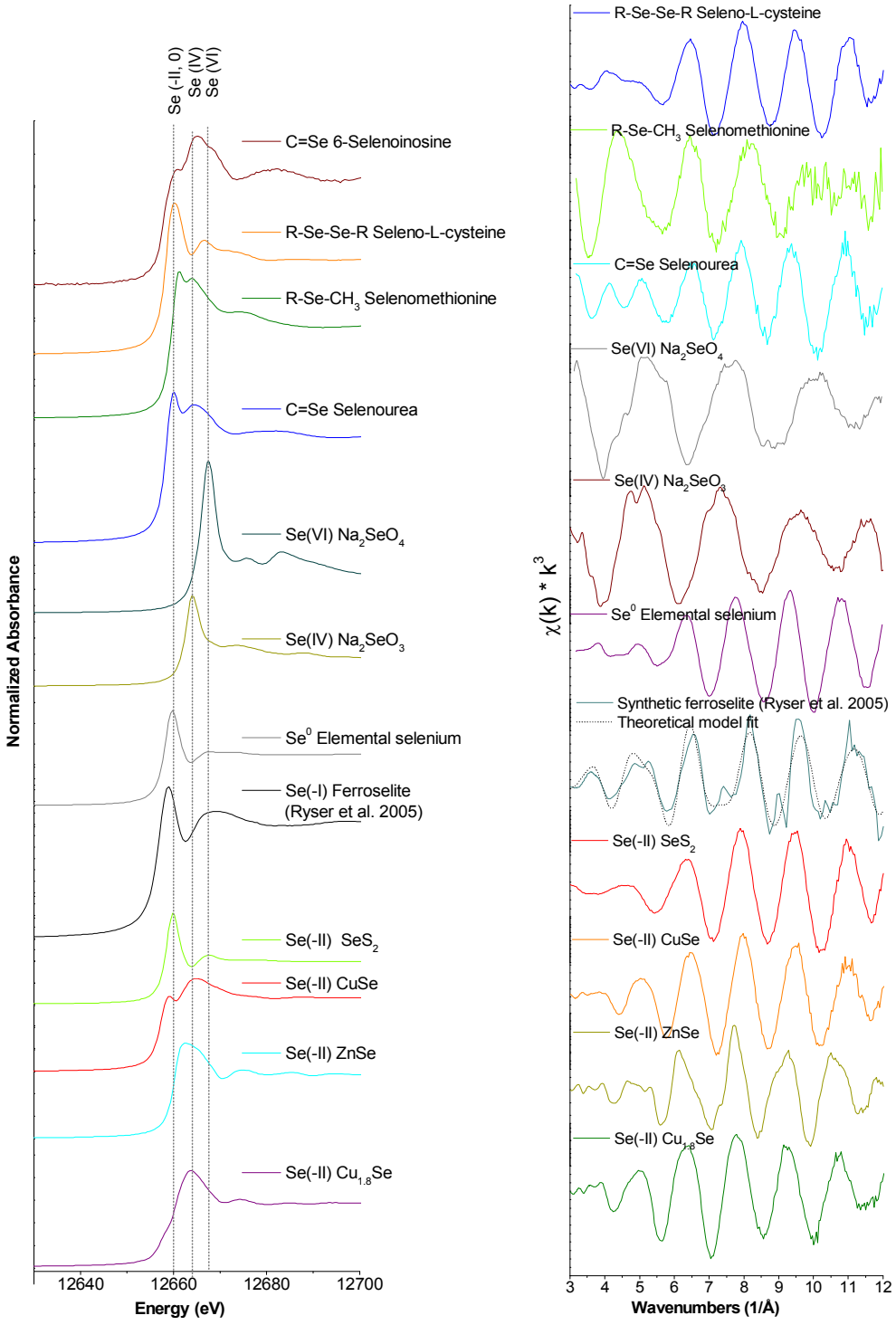

Figure S7 Se K-edge XANES (left) and EXAFS (right) of the standards in the various formal oxidation states analysed in the current study and including the ferroselite ($FeSe_2$) standard from Ryser et al.[23]

Table S10 Se K-edge absorption energies at the inflection point and at the white line peak for the analysed standards including the synthetic ferroselite standard from (*) Ryser et al.[23]

Se standard	Formal oxidation state	Crystal system	First inflection point, eV	Main edge peak, eV
6-Selenoinosine	-II	-	12657.5	12661.0
Seleno-L-cysteine	-II	-	12658.0	12660.2
Selenourea	-II	-	12658.0	12660.2
Selenomethionine	-II	-	12659.2	12661.4
Sodium selenate	VI	Orthorhombic	12665.4	12667.7
Sodium selenite	IV	Monoclinic	12662.3	12663.9
Elemental Se (grey)	0	Trigonal	12658.0	12660.2
Copper selenide	-II	Dihexagonal dypiramidal	12657.1	12664.8
Synthetic ferroselite*	-I	Orthorhombic	12656.3	12659.0
Se sulfide	-II	Cubic	12658.1	12659.7
Berzelianite	-II	Cubic	12659.5	12663.9
Zinc selenide	-II	Cubic	12659.8	12662.7

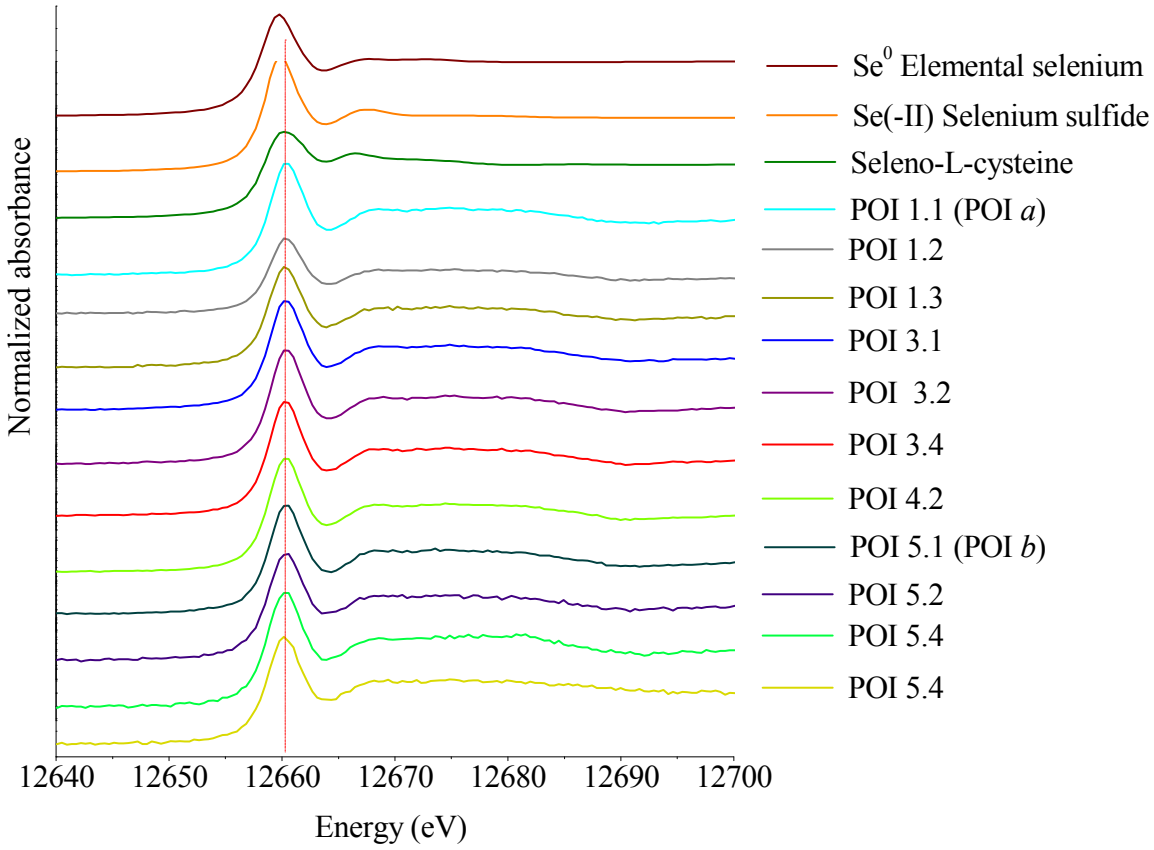

Figure S8. Se K-edge XANES of additional POI analysed in the 5 different mapped areas. All the spectra showed very similar fingerprints with almost identical inflection points and positions of the white lines (where the uncertainty of the data in the XANES region was 0.4 eV). Because of this, and the fact that the Se(-II) sulphide and elemental Se(0) standards are also very similar, it was not possible to differentiate between Se(-II) and Se(0) in POI*a* and POI*b*.

10. Se K-edge EXAFS spectral evaluation procedure.

We fitted the spectra for POI*a* and POI*b* (main manuscript **Figure 3**) in multiple *k* weightings over 3 – 9 $Å^{-1}$ and 4 – 10 $Å^{-1}$, respectively. For POI$a_{euhedral}$ the region in k-space between 9 and 11 $Å^{-1}$ was not included in the fitting procedure as the signal-to-noise ratio was poor.

In the light of our µ-XANES results, several efforts were made to fit the sample spectra to Se coordination environments similar to those in seleno-L-cysteine, selenium sulfide, elemental selenium and ferroselite. Initially, we tried to fit the first shell of the experimental µ-EXAFS

data to models using crystallographic distances for S-C bonds as in seleno-L-cysteine, Se-Se bonds as in elemental Se, and Se-S bond as in selenium sulfide. The spectra could not be fitted with Se-C bonds not even by adjusting σ^2 in the FT, indicating that carbon was unlikely to be the closest neighbouring atom. We carried out other tests using average bond distances for Se-Se in monoclinic Se (i.e., Se-Se= ~2.2Å, Se-Se= 2.5Å and Se-S= ~3.7Å). [24] After adjusting the coordination numbers and σ^2 in the Fourier transform, the spectra visually fit to this theoretical model. However, after refining the σ2 converged into negative values and energy shifted far off indicating an utterly wrong model for the experimental data. After reducing our possibilities to fit the data to the few options given by μ-XANES and the standards, we tried to fit the μ-EXAFS data by using the bond distances for Se-Fe and Se-S bond distances as we knew from μ-XANES data that Se was in a reduced oxidation state (either Se(-I) or Se(-II)). Trials were not straightforward as a single path did not contribute to a single peak in the FT and it was realised the need to fit more than one path in this system using either S or Fe as Ryser et al.[23] also have used. In the process, we tried to the μEXAFS data to the model of ferroselite ($FeSe_2$), pyrite (FeS_2)[26] and even marcasite[26] but attempts to the last one were not successful. We did not try dzharkenite (FeS_2 with Se-Se=2.28 Å reported by Ryser et al.)[23] because from our first trials Se was not the closest neighbouring atom. Therefore, we then tried fitting the μ-EXAFS data to the theoretical single scattering paths of ferroselite ($FeSe_2$)[25] and pyrite (FeS_2)[26].

To do this we calculated the theoretical single (SS) and multiple scattering (MS) paths for the ferroselite and pyrite structures using ATOMS and FEFF in ARTEMIS.[19] We substituted the absorbing atom from sulfur to Se in the calculation of the paths for the pyrite structure. We considered SS and MS paths during the fit tests. However, because of the small contribution of the MS paths within the k-ranges fitted, we only included SS paths in the fits.

For all paths we fixed the amplitude parameter (S_0^2) to 1[23] and constrained the energy shift (ΔE_0) to be the same, the isotropic expansion coefficient (α) and the disorder parameter in the distribution of inter-atomic distances (σ^2) were set as the fitting parameters.

Despite these efforts the attempts we made to fit the μ-EXAFS spectra of the POI*a*$_{euhedral}$ to ferroselite were unsuccessful. Instead these data were fit to the first three 2-leg theoretical SS paths (Se-S=2.18Å, Se-Fe=2.26Å and Se-S=3.07Å) of the pyrite structure including Se as the absorber atom. We initially also included the fourth 2-leg theoretical SS path (Se-S=3.32Å), however it yielded a very large EXAFS σ^2 in the fit and was subsequently discounted. We replaced sulfur with Se in this path with a degeneracy of 6 (as per the theoretical Se-S path) and obtained a better fit, however the best fit was achieved with a degeneracy of 1. The first two SS paths (Se-S and Se-Fe) mutually contributed to the first peak of the Fourier transform, overlapping each other, and the last two paths (Se-S and Se-Se) contributed similarly to the second peak.

Similarly, we tried to fit the POI*b*$_{framboidal}$ μ-EXAFS data using the same theoretical model as above, however the first SS path Se-S (2.18Å) was completely out of position with the first peak in the Fourier transform. We obtained a better fit using four paths of the theoretical structure of ferroselite (Se-Fe=2.35Å, Se-Fe=2.38Å, Se-Se=3.40Å, Se-Se=3.58Å)[25] and one path of the pyrite structure (Se-S=3.07Å).[26] We increased the degeneracy of the Se-Se3 path at 3.58Å to 6 instead of 2, where 2 is the calculated path using the theoretical crystal structure. The Se-S path included in the fit considerably reduced χ^2. The EXAFS σ^2 of the fit were between 0.002 and 0.009 ($Å^2$), which are within the range of expected values. [21] In general, the two fits improved considerably by the addition of every path, with each path addition significantly decreasing the reduced χ^2 and the R-factor. [27]

In addition, we fitted the spectra for both POI in multiple *k* weightings over 3 – 8.5 $Å^{-1}$ (POI*a*) and 4 – 8.5 $Å^{-1}$ (POI*b*) to test our fit results when excluding noisy data at high *k*. On freely refining the fit parameters we found that the distances and Debye-Waller factors were essentially unchanged, indicating comparable Se molecular environments as those shown in Table 3 and Figure 3 in the manuscript, with somewhat improved fit statistics as to be expected (POI*a* R-factor 0.022, reduced χ^2 94; POI*b* R-factor 0.017, reduced χ^2 118).

Figure S9 shows the overlaid experimental data for POI*a* and POI*b*. The spectra are similar over the entire k-space range measured, with spectral features at ~ 4.2, 5.7 and 6.5 $Å^{-1}$ apparent in both spectra. However, the Fourier transforms indicate that Se is not present in exactly the same bonding environment in POI*a* and *b*. For example, POI*a* shows a slightly larger distance than POI*b* in the first coordination shell at ~2 Å (Se-S path 2.344 ± 0.003 for POI*a* and Se-Fe path 2.275 ± 0.004 for POI*b*), at ~ 3 Å POI*a* shows a shorter distance than the POI*b*. **Figure S10** presents the averaged k3-weighted of the spectra for POI*a*, POI*b* and synthetic ferroselite from Ryser et al.[23] The spectra are not identical but they show oscillations in phase between 3 and 9 wavenumbers, there are few differences also represented in the fit. Despite the fact of being ferroselite a synthetic standard, the overall similitude is very good a complex natural sample. **Figure S11** shows the contribution of each path included in the fit to the first and second peak of the FT. It is clear that the Se-Fe paths contribute entirely to the first peak whereas the Se-Se paths contribute to the second peak. The inclusion of Se-S path made the fit far better at the left shoulder of the second peak.

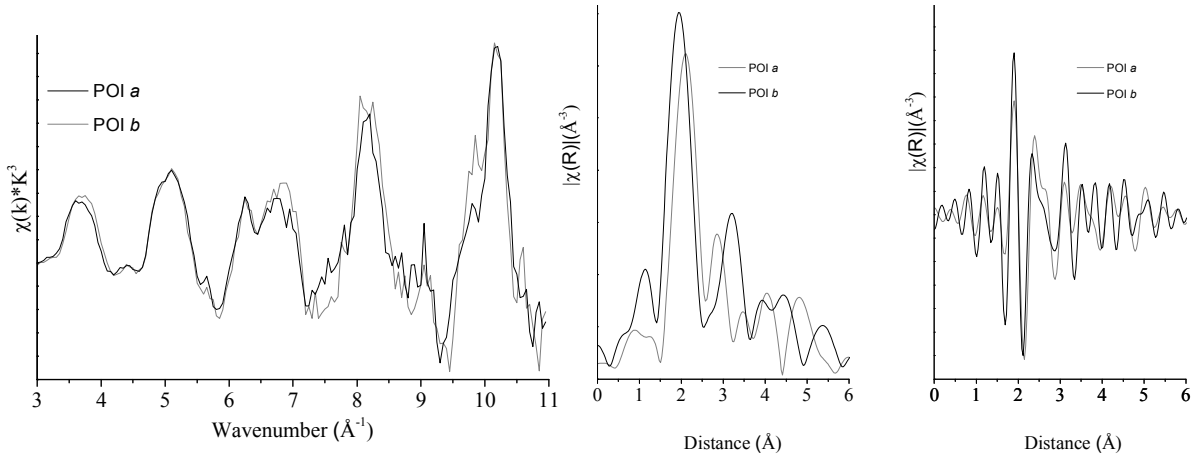

Figure S9 Overlaid experimental data for POI*a* and POI*b*. Averaged k^3-weighted (left), magnitude of the Fourier transform (middle) and real part of the Fourier transform of the spectra using a k-weight of 3 (right).

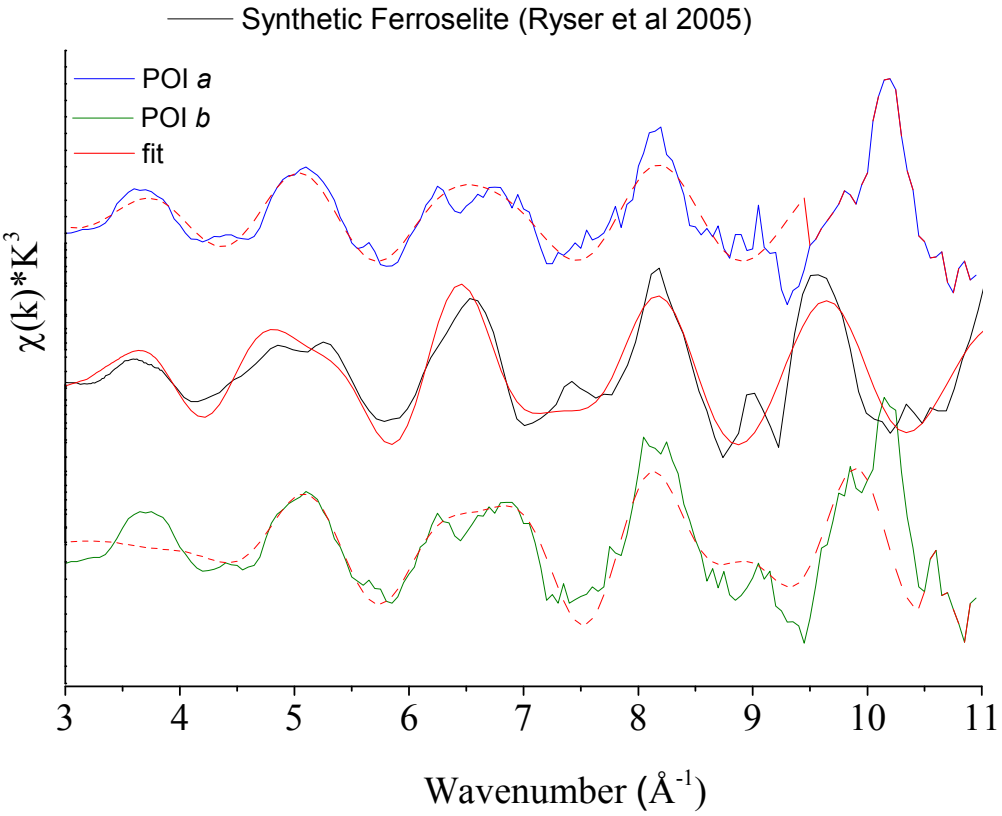

Figure S10 Averaged k3-weighted spectra for POI*a*, POI*b* and synthetic ferroselite from Ryser et al.[23]

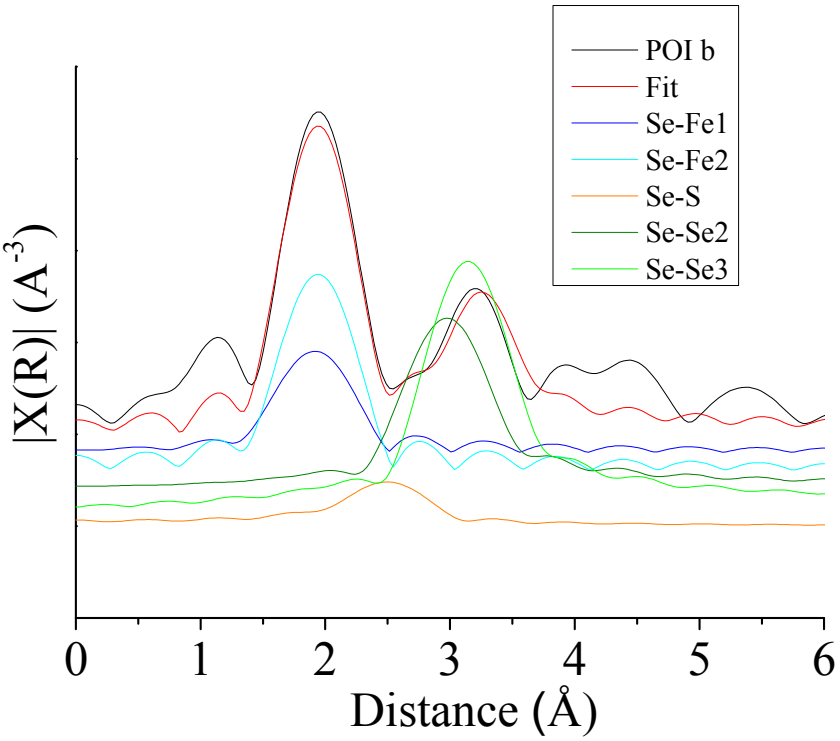

Figure S11 Magnitude of the Fourier transform showing the experimental data for POI b, the fit and the contribution of the scattering paths used to fit the experimental data.

11. Thermodynamic approaches for ferroselite formation.

Using the up to date thermodynamic data for Se species in the geochemical modelling programme Geochemists Workbench[28], we constructed Eh–pH diagrams of Se species in the system Fe-S-Se-H_2O including ferroselite, FeSe, elemental Se and other aqueous Se species. The results suggest that at a very low oxidation potential, in the presence of both S and Fe, pyrite occurs over a wide range of pH (between 2 and 14 - left plot). However, when introducing elemental Se into the system, ferroselite ($FeSe_2$) co-exists with pyrite at low oxidation potentials (**Figure S12**, right plot). This indicates that elemental Se has to be

reduced, and as it becomes less oxidized it combines with dissolved Fe^{+2} forming ferroselite (right). In addition, the diagrams reveal that at more alkaline conditions and very low oxidation potential Se can become stable as an FeSe species. However, even a slight change in redox conditions or pH would lead to the precipitation of $FeSe_2$ or oxidation of the FeSe to elemental Se or dissolution and Se release.

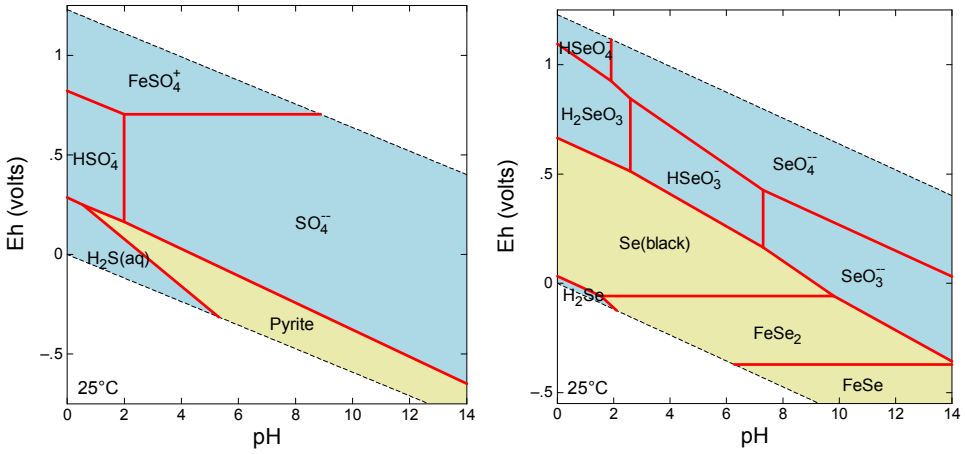

Figure S12 Eh-pH diagram of Se species in the Fe-S-Se-H_2O system including ferroselite, FeSe, elemental Se and other aqueous Se species. (Left): Diagram for the S and Fe species only $[Fe^{+2}] = 10^{-3}$ molar, $[H_2S]=10^{-5}$; (Right): Diagram with the Se species as the base species modelled for $\Sigma[Se]=10^{-5}$ molar and with the same Fe and S conditions.

References

(1) Brumhead D. Geology Explained in the Yorkshire Dales and on the Yorkshire Coast. David and Charles, London. 1979.

(2) Fisher, Q.J., Wignall, P.B. Paleoenvironmental controls on the uranium distribution in an Upper Carboniferous black shale (Gastrioceras listeri Marine Band) and associated strata. *Chem Geol*. **2001**, 175, 605-621.

(3) Wignall, P.B., Newton, R.J., Little, C.T.S. The timing of paleoenvironmental change and cause-and-effect relationships during the early Jurassic mass extinction in Europe, *Am J of Sci*. **2005**, 305, 1014-1032.

(4) Newton, R.J. The Characterisation of Depositional Environments Using Fe, S and C Geochemistry. University of Leeds. 2001.

(5) Wedepohl, K. H. Environmental influences on the chemical composition of shales and clays, in Physics and Chemistry of the Earth, vol. 8, edited by L. H. Ahrens et al., pp. 305-333, Elsevier, New York. 1971.

(6) Tuttle, M.L.W.,Breit, G.N., Goldhaber, M.B. Weathering of the New Albany Shale, Kentucky: II. Redistribution of minor and trace elements. *Appl Geochem*. **2009**, 24, 1565-1578.

(7) Morse, J.W. and Luther, G.W. Chemical influences on trace metal sulfide interactions in anoxic sediments. *Geochim Cosmochim Ac*. **1999**, 63(19-20), 3373-3378.

(8) Deconinck, J. F., Hesselbo, S. O., Debuisser, N., Averbuch, O., Baudin, F., Bessa, J. Environmental controls on clay mineralogy of an Early Jurassic mudrock (Blue Lias Formation, southern England). *Int J Earth Sci*. **2003**, 92, 255-266.

(9) Baioumy, H., Attia, A. E., Boulis, S., Hassan, M., Helmy, M. Rock compostion and origin of late cretaceous shales in the Duwi Formation, Upper Egypt. *J Miner Petrol Sci*. **2003,** 98, 76-86.

(10) Gad, M.A., Catt, J.A., Le Riche, H.H. Geochemistry of the Whitbian (Upper Lias) sediments of the Yorshire Coast. Proceedings of the Yorkshire Geological Society. **1969**, 38, 105-139.

(11) Newton, R.J., Bottrell, S.H., Dean, S.P., Hatfield, D., Raiswell, R. An evaluation of the use of the chromous chloride reduction method for isotopic analyses of pyrite in rocks and sediment. *Chem Geol*. **1995**, 125, 317-320.

(12) Li, Y.H. A compendium of geochemistry: from solar nebula to the human brain. Princenton University Press, Princenton New Jersey. 2000.

(13) Kulp, T.R. and Pratt, L.M. Speciation and weathering of selenium in upper cretaceous Chalk and shale from South Dakota and Wyoming, USA. *Geochim Cosmochim Ac.* 2004, 68(18), 3687-3701.

(14) Lussier C., Veiga, V., Baldwin, S. The geochemistry of selenium associated with coal waste in the Elk River Valley, Canada. *Environ Geol*. **2003**, 44 ,905-913.

(15) Matamoros-Veloza, A., Newton, R.J. and Benning, L.G. What controls selenium release during shale weathering? *Appl Geochem*. **2011**, 26, S222-S226.

(16) Thompson, A. X-ray Data Booklet. Center for X-ray Optics and Advance Light Source. Lawrence Berkeley National Laboratory. University of California. Berkeley. 2009

(17) Sole, A., Papillon, E., Cotte, M., Walter, P.H., Susini, A. A multiplatform code for the analysis of energy-dispersive X-ray fluorescence spectra. *Spectrochim Acta B*. **2007**, 62, 63-68.

(18) Webb, S. SMAK v0.52 Sam's microprobe analysis kit. Standford synchrotron radiation facility. 2006. *http://www.stanford.edu/~swebb*.

(19) Ravel B. and Newville M. ATHENA, ARTEMIS, HEPHAESTUS: data analysis for X-ray absorption spectroscopy using IFEFFIT. *J Synchrotron Radiat*. **2005**, 12, 537–541.

(20) Tenderholt A., Hedman, B. and Hodgson K.O. (2007) Modified Quinn, P. PySpline v.1.3: A modern, cross- platform program for the processing of raw averaged XAS edge and EXAFS data. AIP Conference Proceedings (XAFS13). **2009**, 882 ,105-107.

(21) Binsted, N.; Hasnain, S. S. State-of-the-art analysis of whole X-ray absorption spectra. *J Synchrotron Radiat*. **1996**, 3, 185-196.

(22) Pickering, I.J., Gordone Brown, Jr., Tokunaga, T. Quantitative Speciation of Selenium in Soils Using X-ray Absorption Spectroscopy. *Environ Sci Technol*. **1995**, 29(9), 2456-2459.

(23) Ryser, A.L., Strawn, D.G., Marcus, M.S., Johnson-Maynard, J.L., Gunter, M.E., Moller, G. Micro-spectroscopic investigation of selenium-bearing minerals from the Western US Phosphate Resource Area. *Geochem T*. **2005**, 6(1),1-11.

(24) Calvo, C., Gillespie, R.J.,Vekris, J.E., Ng, H.N. Title Structure of monoclinic sulphur-selenium Se3S5. *Acta Crystallogra B*. **1978**, B34, 911-912.

(25) Bur'yanova Z. and Komkov, A.I. Ferroselite-a new mineral, *Dokl Akad Nauk SSSR.* 1995, 105, 812-813 (Russian); Chemical Abstract. **1955**, 50, 9239.

(26) Brostigen, G. and Kjekshus, A. Redetermined crystal structure of FeS2 (pyrite). *Acta Chem Scand*. **1969**, 23, 2186-2188.

(27) Stern E. A., Newville M., Ravel B., Yacoby Y. and Haskel D. The UWXAFS analysis package: philosophy and details. *Physica B*. **2005**, 208 and 209, 117–120.

(28) Bethke, C.M., Yeakel, S. The Geochemist's Workbench Release 7.0.,GWB Essentials Guide. University of Illinois, Urbana-Champaign,IL. 2008.